

The evolution of a circumplanetary disc with a dead zone

Cheng Chen [★], Chao-Chin Yang (楊朝欽), Rebecca G. Martin and Zhaohuan Zhu

Department of Physics and Astronomy, University of Nevada, Las Vegas, 4505 South Maryland Parkway, Las Vegas, NV 89154, USA

Accepted XXX. Received YYY; in original form ZZZ

ABSTRACT

We investigate whether the regular Galilean satellites could have formed in the dead zone of a circumplanetary disc. A dead zone is a region of weak turbulence in which the magnetorotational instability (MRI) is suppressed, potentially an ideal environment for satellite formation. With the grid-based hydrodynamic code, FARGO3D, we examine the evolution of a circumplanetary disc model with a dead zone. Material accumulates in the dead zone of the disc leading to a higher total mass and but a similar temperature profile compared to a fully turbulent disc model. The tidal torque increases the rate of mass transport through the dead zone leading to a steady state disc with a dead zone that does not undergo accretion outbursts. We explore a range of disc, dead zone and mass inflow parameters and find that the maximum mass of the disc is around $0.001 M_J$. Since the total solid mass of such a disc is much lower, we find that there is not sufficient material in the disc for in situ formation of the Galilean satellites and that external supplement is required.

Key words: methods: numerical – hydrodynamics – accretion, accretion discs – planets and satellites: formation – planets and satellites: composition

1 INTRODUCTION

In our solar system, regular satellites have prograde, nearly circular and nearly coplanar orbits. These regular satellite systems exist around all giant planets, including Uranus and Neptune. These are thought to have formed in a circumplanetary disc during the later stages of the formation of the central giant planet (Canup & Ward 2002, 2006; Mosqueira & Estrada 2003). The formation mechanism for satellites in a circumplanetary disc may be similar to that of planets forming in a protoplanetary disc but on a smaller scale (Pollack et al. 1991). For a sufficiently massive planet that forms in a protoplanetary disc, tidal torques may open a gap within the disc (Lin & Pringle 1987). Gas continues to flow through the gap and a circumplanetary disc forms (Artymowicz & Lubow 1996; Lubow et al. 1999; D’Angelo et al. 2002; Bate et al. 2003). Understanding the physical structure of the circumplanetary disc can help us to explain the formation of the regular satellites.

There were several circumjovian disc models that attempt to explain the formation of the Galilean satellites. Canup & Ward (2002) described a gas starved disc model which allows a satellitesimal to form and condense water ice at low temperatures near the end of disc life time. However, their 1D simulations showed that the disc is orders of magnitude less massive than the minimum-mass subnebula model. The minimum-mass subnebula is a circumjovian

disc that contains the minimum amount of solids necessary to build the Galilean satellites, hence the results of Canup & Ward (2002) imply that there may not have enough material to form the satellites at once. Furthermore, Estrada et al. (2009) used the minimum-mass subnebula and 2D simulations to show that the circumplanetary disc may be too hot for icy satellites to form and survive in the disc.

The tidal truncation from the Sun constrains the size of a circumplanetary disc, which is limited to be about 0.4 times the Hill radius (Martin & Lubow 2011). At this radius, the viscous torque balances the tidal torque from the central star that removes angular momentum at the outer edge of a circumplanetary disc. However, the Galilean satellites around Jupiter lie within a small radius and the outermost satellite, Callisto, is at $0.0345 R_H$. This compact configuration must be explained either by the structure of the disc or the later satellite evolution.

To solve both problems of mass deficiency and disc temperature, Lubow & Martin (2013) suggested that a dead zone in a circumplanetary disc provides a quiescent and cool environment suitable for icy satellite formation. Material in the disc interacts through viscosity that is thought to be driven by the MRI (Balbus & Hawley 1991). This mechanism requires a sufficiently high ionisation level in the disc to operate. Protoplanetary discs are too cold and dense for the MRI to operate throughout (Gammie 1996) and the situation is the same in circumplanetary discs because of their relatively similar temperature but even higher densities than the local protoplanetary disc (Lubow & Martin 2013; Fujii

[★] E-mail: chenc21@unlv.nevada.edu

et al. 2017). The inner regions of a circumplanetary disc are hot enough to be thermally ionised. However, farther from the planet, external sources such as cosmic rays and X-rays from the central star only ionise the surface layers, leaving a dead zone at the disc mid-plane where the MRI can not operate (e.g., Gammie 1996; Gammie & Menou 1998). The dead zone is a quiescent region where solids can settle to the disc mid-plane (e.g., Youdin & Shu 2002; Youdin & Lithwick 2007; Zsom et al. 2011). The surface density may also increase in the dead zone due to the low viscosity. In the case of a protoplanetary disc, planetesimals may form in such a quiescent region (e.g., Bai & Stone 2010; Yang et al. 2018). If the formation mechanism of regular satellites is analogous to planet formation, then satellitesimals could form in the same way in a circumplanetary disc. We note that if the dead zone viscosity is sufficiently small, however, a steady state disc may not exist (Martin & Lubow 2014).

Circumplanetary discs with dead zones may be unstable to accretion outburst cycles (Lubow & Martin 2013) that are similar in nature to the gravo-magneto disc instability that is thought to explain FU Orionis outbursts in young stars (Armitage et al. 2001; Martin & Lubow 2011; Zhu et al. 2009). As the dead zone grows in mass, the temperature increases due to increased viscous heating or gravitational instability, and the MRI may be triggered and cause a sudden increase in the disc turbulence, resulting in an accretion outburst. Some or all of the dead zone region becomes fully turbulent for a short period of time. After the outburst, the dead zone forms again and the cycle continues. The outbursts may cease once the mass infall rate drops off. Since the outburst may lead to the accretion of the embryos of satellites on to the planet (Lubow & Martin 2013), the satellites likely form after the outbursts have finished, or farther out in the disc.

Also noticeable is that there exists large difference in bulk density between inner and outer Galilean satellites, indicating that the water snowline plays an important role in their compositions. Ganymede and Callisto, the two outer satellites, contain about 50 percent ice while the two inner satellites contain much less (Kuskov & Kronrod 2005). The temperature of the snowline is around 170 K if we ignore the effects of dust size and gas density (Hayashi 1981; Lecar et al. 2006). The two outer Galilean satellites were likely formed outside the snowline since they accreted more mass from water ice condensation. The partially differentiated structure of Callisto suggests that its ice never fully melted and that the snowline radius was always inside of its orbit (Lunine & Stevenson 1982; Schubert et al. 2004). The disc temperature depends on the mass accretion rate, and for a fully MRI active disc, the accretion rate must be substantially lower than the accretion rate during the T Tauri period for the snowline radius to be in the middle of the Galilean satellites (Canup & Ward 2002; Estrada et al. 2009). On the other hand, the disc model with a dead zone can have larger accretion rates for a cooler disc (Lubow & Martin 2013). Thus, a comprehensive parameter study is necessary to explain the formation of Galilean satellites by considering the snowline radius.

In this article, we extend the work of Lubow & Martin (2013) who modelled a circumplanetary disc with a dead zone in 1D. We use two-dimensional simulations that allow us to properly take into account the tidal torque from the Sun. In Section 2, we describe our layered disc model for

a circumjovian disc. We show simulation results from fully turbulent disc models in Section 3 and from those models with a dead zone in Section 4. In Section 5, we discuss the implications of our results and potential solutions to the formation of the Galilean satellites in the circumjovian disc. Finally, we draw our conclusions in Section 6.

2 CIRCUMPLANETARY DISC MODEL

We model a circumplanetary disc in 2D with FARGO3D that solves the hydrodynamical equations in the cylindrical coordinate system (R, ϕ) that is centred on the planet (Benítez-Llambay & Masset 2016). The inner boundary is at $R_{\text{in}} = 0.003 R_{\text{H}}$ and the outer boundary is at $R_{\text{out}} = 1.0 R_{\text{H}}$. R_{H} is the Hill radius of Jupiter

In the radial direction we take 256 grid points distributed in logarithmic scale, and in the azimuthal direction we take 128 grid points at regular intervals. We set the mass of the planet M_{p} to be one Jupiter mass, M_{J} , and the coordinate system corotates with the planet. Hence, we put a star with mass $M = 1 M_{\odot}$ at an orbital radius of $R = 14.3 R_{\text{H}} = 5.2 \text{ au}$, which revolves the centre of the grid at an angular frequency of Jupiter's orbit. The Hill radius of Jupiter is

$$R_{\text{H}} = 5.2 \left(\frac{M_{\text{J}}}{3M_{\odot}} \right)^{1/3} \text{ au} \approx 0.36 \text{ au}. \quad (1)$$

The initial surface density is set to be uniform and small, $\Sigma = 0.001 \text{ g cm}^{-2}$. The initial disc aspect ratio is $H/R = 0.05$ everywhere. Therefore, the initial sound speed is

$$c_{\text{s}} = 0.05 \sqrt{\frac{GM_{\text{J}}}{R}} \text{ cm s}^{-1}, \quad (2)$$

where G is the gravitational constant.

The inner and outer radial boundaries have free flow boundary conditions. The density, energy and radial velocity are copied from the last active zones to the ghost zones. Gas can only flow out through the boundary and no gas can flow into the mesh from beyond the inner and outer boundaries. Hence, the radial velocity in the ghost zones are set to be zero when it is toward the active zone. The azimuthal velocities in the ghost zones are set to their local Keplerian velocities.

The energy equation in our model reads

$$\frac{\partial e}{\partial t} + \nabla \cdot (e\mathbf{v}) = -p\nabla \cdot \mathbf{v} + Q_{+} - Q_{-}, \quad (3)$$

where e is thermal energy density (thermal energy per unit area), \mathbf{v} is flow velocity, p is vertically integrated pressure, Q_{+} is a heating source term and Q_{-} is a cooling source term. From this equation, each cell in the mesh grid gains or loses thermal energy because of flow advection, compressional work, viscous heating, and radiative cooling, respectively. The heating term can be written as (Collins et al. 1998; D'Angelo et al. 2003)

$$Q_{+} = \frac{1}{2\nu\Sigma} (\tau_{\text{RR}}^2 + \tau_{\phi\phi}^2 + \tau_{\text{R}\phi}^2) + \frac{2\nu\Sigma}{9} (\nabla \cdot \mathbf{v})^2, \quad (4)$$

where ν is turbulent viscosity and $\tau_{\text{RR}}, \tau_{\phi\phi}$ and $\tau_{\text{R}\phi}$ are the components of the viscous stress tensor in radial-radial, azimuthal-azimuthal and radial-azimuthal directions. The

cooling is determined by black body radiation near the surface of the disc

$$Q_- = \sigma T_e^4, \quad (5)$$

where σ is the Stefan-Boltzmann constant and T_e is the effective temperature. The effective temperature is related to the mid-plane temperature, T_c , by

$$T_c^4 = \tau T_e^4, \quad (6)$$

where the optical depth is

$$\tau = \frac{3}{8} \kappa \frac{\Sigma}{2}, \quad (7)$$

and the opacity is $\kappa = a T_c^b$, where T_c is in Kelvin. In our model, we take $a = 0.02 \text{ cm}^2 \text{ g}^{-1}$ and $b = 0.8$ assuming that dust dominates the absorption properties of matter in the disc (Bell & Lin 1994; Zhu et al. 2009). The mid-plane disc temperature is derived from the internal energy via

$$e = \frac{\Sigma R T_c}{(\gamma - 1) \mu}, \quad (8)$$

where $\gamma = 5/3$ is the adiabatic index and R is the gas constant. Most of the mass of the disc is in molecular hydrogen so the mean molecular weight is $\mu = 2.4 \text{ g mol}^{-1}$ (Dutrey et al. 2014).

We adopt the layered disc model of Armitage et al. (2001) and assume a spatially varying turbulent viscosity ν that depends on the local condition of the disc (see also Zhu et al. 2009; Martin & Lubow 2011; Martin & Livio 2012). The critical surface density, Σ_{crit} , and the critical disc temperature, T_{crit} , are the two constants we use to determine if a location is fully MRI active or contains a dead zone, as discussed below.

The disc is ionised by external sources, such as cosmic rays or X-rays. For a lower disc surface density, $\Sigma < \Sigma_{\text{crit}}$, the gas is fully MRI active, where the ionising sources can penetrate deep into the mid-plane. However, the value of the critical surface density Σ_{crit} is uncertain. For discs around T Tauri stars, at a radial distance less than 0.1 au where cosmic rays ionise effectively, the critical surface density is $\Sigma_{\text{crit}} \approx 100 \text{ g cm}^{-2}$ (Umebayashi & Nakano 1981). If chemical reactions of charged particles are taken into account, this value could be lower (Sano et al. 2000). The MRI could operate in a disc ionised by stellar X-rays with $\Sigma_{\text{crit}} \approx 1 - 30 \text{ g cm}^{-2}$ (Turner & Sano 2008; Bai & Goodman 2009). In the circumjovian disc, Fujii et al. (2014) found the MRI can only be sustained if the surface density is below 10 g cm^{-2} for the region around the Galilean satellites. Due to the uncertainty, we let Σ_{crit} be a free parameter that is in the range of $1 - 10 \text{ g cm}^{-2}$.

For disc temperature $\gtrsim 800 \text{ K}$, collisional ionisation of potassium makes the ionisation fraction increases exponentially with temperature (Umebayashi 1983) and thus we take this temperature to be the critical above which MRI can operate. In other words, when $T > T_{\text{crit}}$, the gas is fully MRI active no matter how large Σ is. Therefore, if a region in a disc has $\Sigma > \Sigma_{\text{crit}}$ and $T < T_{\text{crit}}$, a dead zone around the mid-plane forms and the viscosity in the dead zone is much lower than that in a fully MRI turbulent region because of the inefficient transport of angular momentum.

The viscosity in the fully MRI active parts of the disc is parametrized by the Shakura & Sunyaev (1973) α parameter

$$\nu = \alpha c_s H, \quad (9)$$

where the sound speed $c_s = \sqrt{RT_c/\mu}$ and H is the vertical scale height of the gas. Observations of FU Orionis suggested that $\alpha \approx 0.01$ (Zhu et al. 2007). Observations of X-ray binaries and dwarf novae that have a fully turbulent disc gave an estimate of $\alpha \approx 0.1 - 0.4$ (King et al. 2007; Martin et al. 2019). MHD simulations found $\alpha \sim 0.01$ although those models depends on numerous parameters such as the net magnetic flux (e.g., Hawley et al. 1995; Johansen et al. 2006; Yang et al. 2009; Bai & Stone 2013), stratification (Davies et al. 2010; Bodo et al. 2014; Ryan et al. 2017) and treatments of small-scale dissipation (Fromang et al. 2007; Oishi & Mac Low 2011; Meheut et al. 2015; Walker et al. 2016). In this work, we assume the α parameter in a fully MRI turbulent region to be 0.01. In regions with a dead zone, the viscosity is approximated with

$$\nu = \alpha_{\text{dz}} c_s H, \quad (10)$$

where the parameter α_{dz} is much smaller than α but may not be zero since there are several possible mechanisms to drive turbulence in the dead zone. First, hydrodynamic instabilities such as the baroclinic instability may operate in the dead zone (e.g., Klahr & Bodenheimer 2003; Petersen et al. 2007; Lesur & Ogilvie 2010). A pressure gradient over surfaces of constant density can generate vorticity leading to $\alpha \approx 5 \times 10^{-3}$ (Lyra & Klahr 2011). Second, shearing box simulations showed that MHD turbulence generated in the disc surface layers can penetrate into the mid-plane and exert a non-zero Reynolds stress there (Fleming & Stone 2003; Oishi et al. 2007; Turner et al. 2007; Oishi & Mac Low 2009; Okuzumi & Hirose 2011). Finally, self-gravity can also produce turbulence in the mid-plane of the disc (e.g. Lodato & Rice 2004). The turbulence driven by self-gravity can be up to $\alpha \sim 0.1$ (Shi & Chiang 2014). However, self-gravity is unlikely to play a role in the circumplanetary disc (Martin & Lubow 2014) and we do not consider this effect in our work. In any case, there are still some uncertainties for the turbulent transport in the dead zone and we set the viscosity parameter in the dead zone to be a constant in the range of $\alpha_{\text{dz}} = 10^{-5}$ to 10^{-3} .

We note that the region of the disc with a dead zone should ideally be modelled with a vertically varying α viscosity parameter (e.g. Pierens & Nelson 2010) based on fits to MHD simulations (e.g. Okuzumi & Hirose 2011; Gressel et al. 2011; Uribe et al. 2011, 2013). However, since we use 2D simulations in $R - \phi$, we do not model the vertical structure of the disc. Instead, we consider α as a density-weighted, vertically integrated quantity to model the radial flow through the disc (e.g. Suzuki et al. 2010, 2016) and leave it as a free parameter (Section 4.3). This approximation is reasonable as long as the column density of the active layer is much smaller than the column density in the dead zone layer. Since the active layer is generally small (e.g. Martin et al. 2012a,b; Fujii et al. 2014), this approximation does not significantly affect the disc mass in our steady-state models. In the case of a much smaller dead zone size, our models represent the upper limit to the disc mass.

We note that density waves in the circumplanetary disc can also drive disc accretion. Zhu et al. (2016) found that the tidal torque from the Sun can excite spiral density waves in the circumjovian disc and it results in shocks that transport angular momentum through the disc. Thus, the effective viscosity parameter in a dead zone may be larger than α_{dz} .

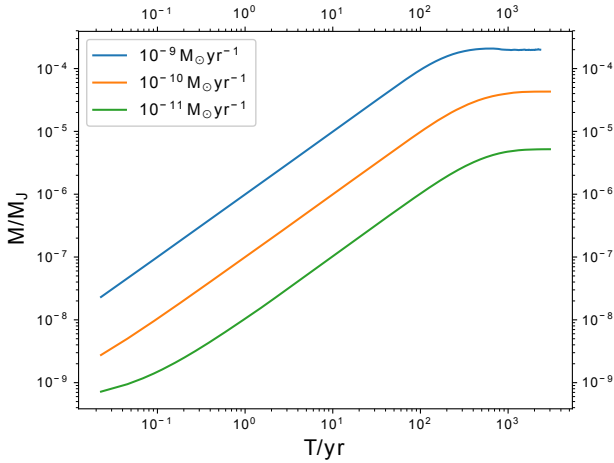


Figure 1. The total mass of the fully MRI turbulent disc models S1 ($\dot{M} = 10^{-9} M_{\odot} \text{yr}^{-1}$), S2 ($\dot{M} = 10^{-10} M_{\odot} \text{yr}^{-1}$) and S3 ($\dot{M} = 10^{-11} M_{\odot} \text{yr}^{-1}$) as a function of time.

Their simulations showed that the effective viscosity value is in the range $10^{-4} \leq \alpha_{\text{eff}} \leq 10^{-2}$ in a circumjovian disc. In our 2D simulations, the tidal torque is self-consistently included and may produce a comparable α_{eff} in the disc.

To model the mass accretion from the protoplanetary disc onto the circumplanetary disc, we continuously deposit gas mass at a constant rate over all values of ϕ at a radius of $R_{\text{add}} = 0.33 R_{\text{H}}$ which is the radius determined by the angular momentum of the material that falls into the Hill sphere (Quillen & Trilling 1998; Estrada et al. 2009). We assume that the mass infall rate \dot{M} is similar to that in a protoplanetary disc and hence we consider \dot{M} in the range of $10^{-11} - 10^{-9} M_{\odot} \text{yr}^{-1}$ (Bate et al. 2003; Lubow & D’Angelo 2006; Ayliffe & Bate 2009; Zhu et al. 2016) (See Lubow & Martin (2012) for more discussion).

The fully MRI turbulent disc may evolve differently compared to a disc with dead zone. Strong turbulence leads to a lower surface density and a higher temperature. Thus, it may result in satellites being hard to form in a disc. In the next two sections we describe the results of fully MRI turbulent disc simulations and then our disc models with a dead zone. In Table 1, we summarise all of the simulation parameters.

3 FULLY MRI TURBULENT DISC MODELS

First we consider fully MRI turbulent disc models with $\alpha = 0.01$ everywhere. Fig. 1 shows the total mass of each disc as a function of time for three different infall accretion rates, $\dot{M} = 10^{-9} M_{\odot} \text{yr}^{-1}$ (model S1), $\dot{M} = 10^{-10} M_{\odot} \text{yr}^{-1}$ (model S2) and $\dot{M} = 10^{-11} M_{\odot} \text{yr}^{-1}$ (model S3). Each model is run until it reaches a steady state. The disc initially builds in surface density due to the mass accretion from the outer disc. The disc temperature also increases due to viscous heating (Eq. 4). The viscosity increases with increasing disc temperature and the disc spreads outwards until the disc reaches a quasi-steady state.

Fig. 2 shows the surface density and temperature profiles at time $t = 3000 \text{yr}$. The disc spreads outwards but around a radius of about $0.4 R_{\text{H}}$, where the tidal torque from

the Sun exceeds the viscous torque. Consequently, the tidal torque truncates the disc there (see also Martin & Lubow 2011).

These simulations show that a fully MRI turbulent disc model is inadequate to explain the formation of the Galilean satellites. The higher the infall accretion rate, the larger the mass of the steady disc. For the highest mass infall rate $\dot{M} = 10^{-9} M_{\odot} \text{yr}^{-1}$ (model S1), the total gas mass of the disc is comparable with the total mass of the Galilean satellites ($\sim 2 \times 10^{-4} M_{\text{J}}$). The solid mass density in the disc is much smaller than the mass of the satellites since the dust-to-gas ratio in a protoplanetary disc is only 1 - 10% (e.g. Soon et al. 2019). Dust drifts from the outer gap region of a protoplanetary disc and the positive gas pressure gradient produced by the gap dams most of the pebble-sized dust. Because most dust has already grown to the size of pebbles when it reaches the region around gas giants, it is dammed at the outer edge of the gap (Lambrechts & Johansen 2012; Okuzumi et al. 2012; Sato et al. 2016). Thus, the dust-to-gas mass ratio is thought to be $< 1\%$ in a circumplanetary disc (Adachi et al. 1976; Zhu et al. 2012). Furthermore, the disc temperature is above the snowline temperature within the region of the Galilean satellites and therefore the temperature is too hot to explain the formation of icy satellites.

On the other hand, for the lower mass infall rates $\dot{M} \lesssim 10^{-10} M_{\odot} \text{yr}^{-1}$ (models S2 and S3), the temperature around the orbital location of Callisto is below the snowline temperature, and water ice may condense there. However, the total masses in these two models ($4.3 \times 10^{-5} M_{\text{J}}$ and $5.2 \times 10^{-6} M_{\text{J}}$) are not high enough for the Galilean satellites to form and grow to their current masses.

Fig. 3 shows the surface density of model S2 in 2D at time $t = 3000 \text{yr}$. Our models show prominent density wave structures in the circumplanetary disc that are not present in the 1D models of Canup & Ward (2002) and Lubow & Martin (2013). The density waves are excited in the vicinity of the Lindblad resonance due to the tidal torques from the Sun, and torques are exerted on the disc at radii where the waves damp (Goldreich & Tremaine 1979).

Because the fully MRI turbulent disc is either not sufficiently massive or too hot to explain the formation of the Galilean satellites in situ, we now consider disc models with dead zones that allow a high surface density to accumulate while remaining cool enough for icy satellite formation.

4 DISC MODELS WITH A DEAD ZONE

In this Section we first consider the evolution of a fiducial disc model with a dead zone and then we vary different disc parameters to understand their effects on the disc evolution and satellite formation.

4.1 Fiducial disc model with a dead zone

We use a fiducial model (model D1) with the same parameters as model R9 in Lubow & Martin (2013) except $\alpha_{\text{dz}} = 10^{-4}$ and $\Sigma_{\text{crit}} = 1 \text{g cm}^{-2}$. The mass infall rate is $\dot{M} = 10^{-10} M_{\odot} \text{yr}^{-1}$ and $\alpha = 0.01$. The blue lines in Fig. 4 show the surface density and the temperature profiles of the disc at time $t = 10000 \text{yr}$. The blue line in Fig. 5 shows the evolution of the total disc

Table 1. The parameters of the simulations. Column 1 is the name of the simulation. Column 2 is the mass infall rate on to the circumplanetary disc. Column 3 is the critical surface density. Column 4 is the viscosity α parameter in MRI active regions. Column 5 is the viscosity parameter in the dead zone, α_{dz} . Column 6 is the simulation end time. Column 7 is the mass of the disc at the end of the simulation. Column 8 is the snow line radius at the end of the simulation.

Model	\dot{M} ($M_{\odot} \text{yr}^{-1}$)	Σ_{crit} (g cm^{-2})	α	α_{dz}	Simulation time (yr)	Mass of disc (M_J)	Snowline radius (R_H)	Resolution (R, ϕ)
S1	10^{-9}	-	0.01	-	3000	2.0×10^{-4}	7.0×10^{-2}	256, 128
S2	10^{-10}	-	0.01	-	3000	4.3×10^{-5}	2.5×10^{-2}	256, 128
S3	10^{-11}	-	0.01	-	3000	5.2×10^{-6}	7.0×10^{-3}	256, 128
D1	10^{-10}	1	0.01	10^{-4}	10000	3.9×10^{-4}	2.4×10^{-2}	256, 128
C1	10^{-10}	10	0.01	10^{-4}	10000	4.0×10^{-4}	2.5×10^{-2}	256, 128
A1	10^{-10}	1	0.01	10^{-3}	10000	1.8×10^{-4}	2.9×10^{-2}	256, 128
A2	10^{-10}	1	0.01	10^{-5}	10000	5.2×10^{-4}	2.7×10^{-2}	256, 128
M1	10^{-9}	1	0.01	10^{-4}	4000	1.0×10^{-3}	6.8×10^{-2}	256, 128
M2	10^{-11}	1	0.01	10^{-4}	17000	1.4×10^{-4}	5.7×10^{-3}	256, 128
H1	10^{-10}	1	0.01	10^{-4}	6300	3.9×10^{-4}	2.3×10^{-2}	512, 256

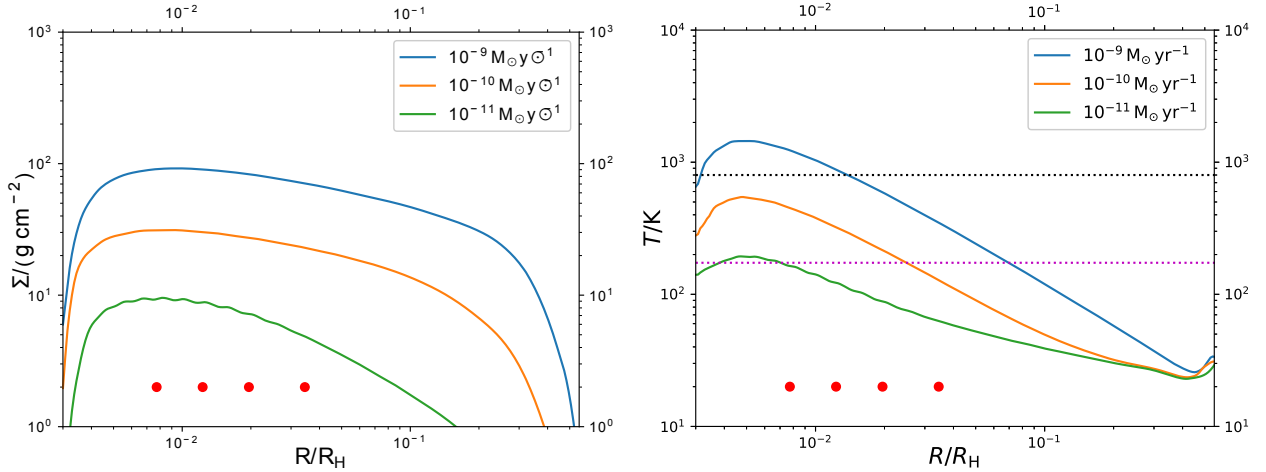


Figure 2. Steady-state, fully MRI turbulent circumplanetary disc models with mass infall rates $\dot{M} = 10^{-9}$ (blue lines), 10^{-10} (orange lines) and $10^{-11} M_{\odot} \text{yr}^{-1}$ (green lines) at time $t = 3000 \text{yr}$. Left panel: Surface density. Right panel: Temperature. The black dotted line is the critical temperature $T_{\text{crit}} = 800 \text{K}$ and the purple dotted line is the snowline temperature, $T_{\text{snow}} = 170 \text{K}$. The four red dots represent the orbital locations of Io ($R = 0.0077 R_H$), Europa ($R = 0.0123 R_H$), Ganymede ($R = 0.0196 R_H$) and Callisto ($R = 0.0345 R_H$).

mass in time. The dead zone builds up in mass and expands outwards. Due to the tidal torque, the disc is truncated around $0.4 R_H$. The steady state mass of the disc is almost an order of magnitude larger than that of the fully MRI active disc with the same infall accretion rate (model S2), but the temperature of the disc remains similar to that in model S2.

The tidal torque increases the effective viscosity in the dead zone. Due to the density waves, the disc forms five local peaks in surface density. More specifically, those peaks are formed due to some nonlinear properties of the spirals which are related to the $m=2$ lindblad resonances. They roughly correspond to where the torque density is highest, but themselves are not spirals. Therefore, the depth of the density peak has no direct association with the intensity of the spiral.

Satellitesimals may be trapped and grow in the peaks. The temperatures of two outer peaks are below the snowline temperature and provide an ideal environment to form

Ganymede and Callisto with abundant water ice. Eventually, satellitesimals at the outer peaks migrate inward to the current locations of Ganymede and Callisto. On the other hand, the two inner peaks have temperatures above the snowline temperature. This may explain why Io and Europa contain no water ice or only a little water ice. Thus, the temperature difference between inner peaks and outer peaks can result in the different compositions for the inner and outer Galilean satellites.

The total mass of the disc approaches a steady state value. Thus, even though there is a dead zone within the disc, material is able to flow through it because of the effective viscosity driven by the tidal torques. Material does not continue accumulating in the dead zone as it did in the 1D models of Lubow & Martin (2013). There is a limit to the amount of mass that the circumplanetary disc may contain even with a dead zone. In this model we do not expect outbursts to occur where the MRI is triggered in the dead zone since there is no local peak in the temperature profile

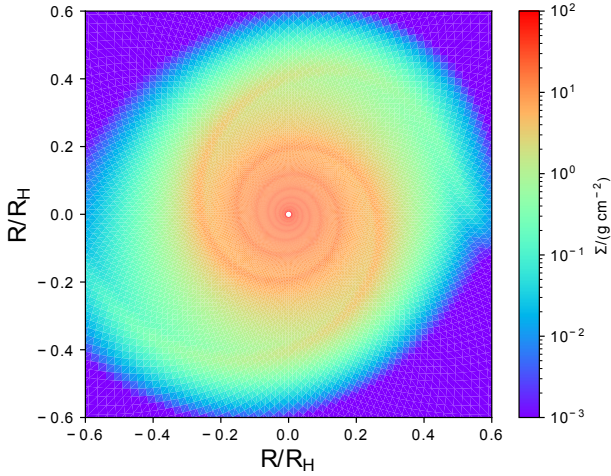


Figure 3. Surface density of steady-state, fully MRI turbulent disc at time $t = 3000\text{yr}$ (S2 model with infall accretion rate $\dot{M} = 10^{-10} M_{\odot} \text{yr}^{-1}$). The sun is 5.2 au away ($14.3 R_H$) on the right hand side of the figure.

that can reach the critical temperature. The total mass of the steady state gas disc is comparable to the total mass of the Galilean satellites (about $4 \times 10^{-4} M_J$).

4.2 Effect of the critical surface density

In this section, we consider how the critical surface density below which the gas is sufficiently ionised by external sources for the MRI to operate affects the circumplanetary disc evolution. We run a simulation with the same parameters as our fiducial disc model but with a higher critical surface density $\Sigma_{\text{crit}} = 10 \text{g cm}^{-2}$. The orange lines in Fig. 4 and in Fig. 5 show the surface density and the disc temperature profiles in steady state and the evolution of total disc mass of model C1. The surface density is similar to that of the fiducial model D1 because the surface density in the steady state is much higher than the critical surface density and the dead zone is largely unaffected. Therefore, the total mass of the disc is similar to model D1. The innermost region of the disc ($r \leq 10^{-2} R_H$) has a higher disc temperature than in model D1 and is slightly depleted, but most of the disc is similar. Thus, the critical surface density has little influence for the circumplanetary disc evolution unless the critical surface density is too high for a dead zone to form in a circumplanetary disc.

4.3 Effect of the viscosity in the dead zone α_{dz}

We now explore the effect of changing the viscosity in the dead zone. This viscosity may be induced by hydrodynamic instabilities or perturbations driven by the surface turbulent layers, as discussed in Sec 1.

4.3.1 Higher α_{dz}

Model A1 has the same parameters as the fiducial model except for a larger $\alpha_{dz} = 10^{-3}$. The green lines in Fig. 4 and in Fig. 5 show the surface density and the disc temperature profiles in steady state and the evolution of the total disc

mass of model A1. The surface density and the disc mass are lower than the fiducial model by a factor of about 2.5 due to the larger α_{dz} that allows material to be transported efficiently and prevents the disc surface density from building up. In addition, there is no density bump in this model as a result. The temperature profile is similar to that in model D1 but is smoother. The temperature around Callisto is below the snowline temperature but the disc around Ganymede has higher temperature than the snowline temperature. For Ganymede and Callisto, they could form in the outer dead zone where abundant water ice exists and then migrate inward to their current locations. However, the disc mass in this model is much too low for the satellites to form.

4.3.2 Lower α_{dz}

Model A2 has the same parameters as the fiducial model D1 except a smaller $\alpha_{dz} = 10^{-5}$. The red lines in Fig. 4 and in Fig. 5 show the surface density and the disc temperature profiles in steady state and the evolution of the total disc mass of model A2. There are six density bumps in the surface density profile and the amplitudes of them are more prominent than those in the fiducial model. The structure is similar to low disc accretion rate models in Zhu et al. (2016) which are inviscid (see their figure 5). Due to the smaller α_{dz} , the total mass of the disc is $5.2 \times 10^{-4} M_J$ and is slightly higher than the fiducial model. The temperature profile is similar to the fiducial model even though the disc has a smaller α_{dz} because the effective α viscosity driven by the density waves is comparable to 10^{-4} . The three outer peaks are below the snowline temperature. Thus, satellitesimals may be trapped and grow in those peaks which may be an ideal environment for ice satellites. However, the total mass of the disc remains too small for the disc to have sufficient solid mass to form the satellites.

4.4 Effect of the mass infall rate

4.4.1 Higher mass infall rates

Model M1 has the same parameters as our fiducial disc model but with a higher mass infall rate of $\dot{M} = 10^{-9} M_{\odot} \text{yr}^{-1}$. The purple lines in Fig. 4 and in Fig. 5 show the surface density and the disc temperature profiles in steady state and the evolution of the total disc mass of model M1. The disc reaches a steady state after a time of about 1800yr. The total disc mass is almost an order of magnitude higher than the fiducial model and about three that of the Galilean satellites. The dead zone forms farther out than the fiducial model, outside of the orbit of Europa. There are three density bumps in the dead zone. However, the temperature is too high for water ice to condense around Ganymede and Callisto in the innermost density bump. If the two outer Galilean satellites can form in the outer two peaks, they might be able to condense water ice there since the disc temperature there is lower than that at their current locations. This scenario is similar to model A of the Galilean satellites formed by pebbles in Shibaike et al. (2019) in which three outer Galilean satellites formed in order at the disc radius $0.065 R_H$ and then migrated inwards to their current locations. The second density bump is close to the snow line temperature. It may help to explain the melted structure of

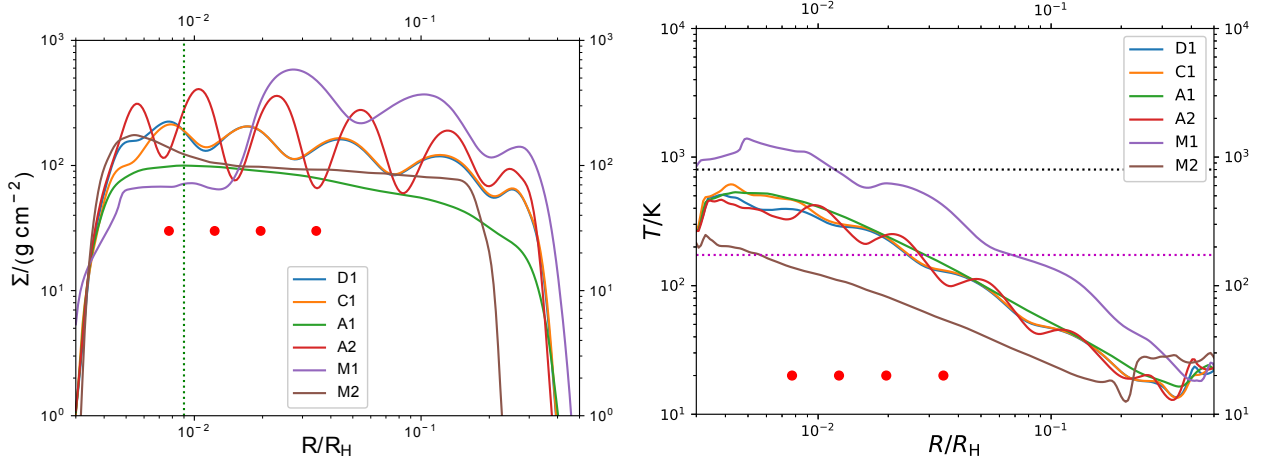


Figure 4. Left: Surface density of the models with a dead zone. Right: Disc temperature of the models with a dead zone. The horizontal black dotted line is the critical temperature $T_{\text{crit}} = 800\text{ K}$ and the horizontal purple dotted line is the snow line temperature, $T_{\text{snow}} = 170\text{ K}$. The red dots show the location of the four Galilean satellites. The snapshots are shown at 10000 yr for D1, C1, A1 and A2, 3800 yr for M1 and 170000 yr for M2.

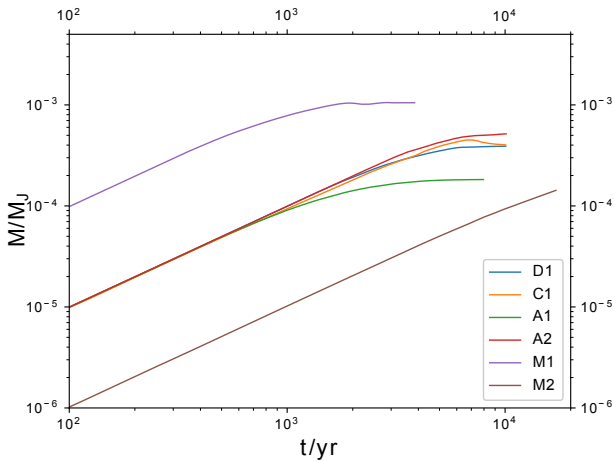


Figure 5. The total mass of the disc for dead-zone models D1, C1, A1, A2, M1 and M2 as a function of time.

Ganymede. They would then migrate inward to their current locations.

There are no accretion outbursts even in the disc with high mass infall rate, in contrast to previous 1D simulations (Lubow & Martin 2012). The outburst can only occur if sufficient material is able to build up in the dead zone to drive viscous heating and trigger the MRI. However, because the tidal torque drives an effective viscosity in the dead zone, the disc reaches a steady state rather than continues to increase in mass.

4.4.2 Lower mass infall rates

Model M2 has the same parameters as the fiducial model except a lower mass infall accretion rate of $\dot{M} = 10^{-11} M_{\odot} \text{ yr}^{-1}$. The brown lines in Fig. 4 and in Fig. 5 show the surface density and the disc temperature profiles near the end of the simulation and the evolution of the total disc mass of model M2. Because the disc is still building up at 17000

yr, the surface density profile and total disc mass are lower than fiducial model by a factor of 3. The disc temperature is much lower than the fiducial model and the whole region around Galilean satellites is below the snowline temperature. However, extrapolating the brown line in Fig. 1, it takes about 10^5 yr for the disc to reach the mass of the disc of model D1. Due to the longer timescale of build up of the disc, it is even more difficult to explain the formation of Galilean satellites in this model.

4.5 Effect of the resolution

Numerical viscosity could modify the accretion rate on to the disc significantly (e.g. Kley 1999; Ochi et al. 2005). To investigate the effect of the resolution, we run the fiducial model (D1) with double the resolution in both R and ϕ in model H1, with otherwise the same parameters. Because this simulation is more expensive than others, we just run it to $t = 6300$ yr. To make a clear comparison, the upper two panels of Fig. 6 show the density and temperature profiles of models D1 and H1. They are shown at the same instant of time $t = 6300$ yr. The surface densities of the two models are similar to each other except that density bumps of model H1 are slightly shallower than model D1. The temperatures of the two models are also similar to each other but the temperature of model H1 is slightly higher than model D1 within $R \approx 0.02$. The lower panel of Fig. 6 shows the evolution of the total disc mass of models D1 and H1. There is a turning point at $t \sim 4000$ yr on the black line, indicating that the disc of model H1 begins to reach a quasi-steady state. It appears that the evolution of the total disc mass of model H1 converges to that of model D1 when extrapolated with time. Thus, despite using a low resolution in the outer disc in our simulations, the effect of numerical viscosity is not significant and the results from our steady-state models should be representative.

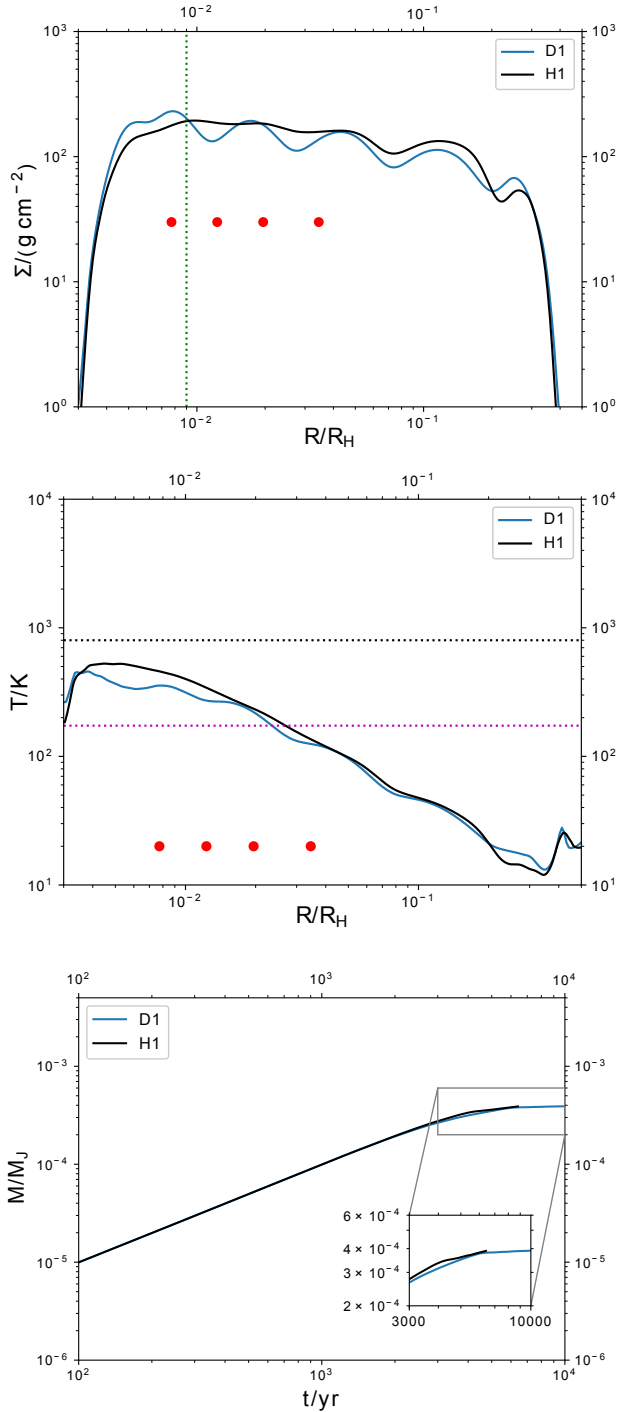


Figure 6. Upper and middle panels: The surface density and disk temperature of models D1 and H1 similar to Fig. 4 except that they are shown at the same time of $t = 6300$ yr. Lower panel: The total mass of the disc for dead-zone models D1 and H1 as a function of time.

5 DISCUSSION

In this work we have modelled the evolution of a circumplanetary disc and drawn some conclusions about satellite formation. We have found that a circumplanetary disc model with a dead zone does not contain sufficient material to form the Galilean satellites all at once. Canup & Ward (2002)

suggested that a solution to this problem is that the solid material does not need to be present all at once, but needs to be processed through the disc over time. Hydrodynamical simulations suggest that the material that flows on to the circumplanetary disc comes from the upper layers of the protoplanetary disc (Machida et al. 2008; Tanigawa et al. 2012; Morbidelli et al. 2014; Szulágyi et al. 2014). These layers are depleted in large dust grains (Paardekooper & Mellema 2006; Paardekooper 2007; Birnstiel et al. 2011) and thus it is difficult to build up sufficient solids to form the Galilean satellites in this way.

Furthermore, we have not included satellite-disc interactions that should be taken into account when satellitesimals form and grow in the circumplanetary disc (Ward 1997; Lubow & Ida 2010). In the high surface density disc, the orbit of the growing satellitesimal may undergo type-I or type-II migration by satellite-disc interactions (Goldreich & Tremaine 1980). The type-I migration time-scale can be quite short for the Galilean satellites, around 10^2 yr (Canup & Ward 2002). However, in a recent study, the Galilean satellites can lock into mean motion resonances during their migration and their orbits become stable after 10^4 yr (Moraes et al. 2018). Besides, the dead zone allows a lower-mass object to open a gap which leads to a much slower type-II migration, because the viscous gap-opening criterion is proportional to α (Goldreich & Tremaine 1980). Moreover, satellitesimals may have much longer time scales of type-I migration due to uncertain corotation torque (see, e.g., Baruteau et al. 2014). For Callisto, to release the gravitational binding energy to prevent the interior temperature from heating to the water sublimation temperature, the migration time scale should be $> 10^5$ yr (Canup & Ward 2002).

Lindblad resonances may play a role when a satellite opens a gap in the disc (Canup & Ward 2002; Lubow & Martin 2013). Once a planet opens a gap, the excitation of the eccentricity of the planet due to the first-order Lindblad resonance has been widely studied (Goldreich & Sari 2003; Ogilvie & Lubow 2003) and this resonance is sensitive to how clean and large the gap is. Nevertheless, at late times when the accretion rate falls off, $\dot{M} \lesssim 10^{-11} M_\odot \text{yr}^{-1}$, the surface density around the Galilean satellites may drop to less than the critical density, thus the disc becomes fully MRI turbulent and masses of satellitesimals may not reach the gap-opening criterion. The available gas at this stage may be sufficient to damp eccentricities developed (Lubow & Martin 2013) and the evidence that the Galilean satellites have low eccentricities (< 0.01) show those satellites have never undergone large excitations. Moreover, to prevent the high temperature around the innermost region of the dead zone, the Galilean satellites may form farther out than their current locations and then migrate inwards later on. In future work, we will use N -body simulations to test whether satellitesimals can survive in different models and migrate inward to their current locations.

Gressel et al. (2013) used 3D global hydrodynamic simulations and found that a circumplanetary disc may be tilted to the orbital plane of the planet by up to about 10° . A tilted disc may affect the accretion of material on to the circumplanetary disc. However, in our simulations we have added the material at a radius corresponding to its angular momentum and thus the location of the mass deposition is unaffected by the disc tilt. Accretion of material may still

be in the plane of the orbit of the planet and thus accretion causes a damping of the tilt. Another difference with a tilted disc is that the tidal torque decreases with tilt. The torque is weakened by a factor of about two for a disc inclination of $i = 30^\circ$ and by a factor of about 20 for $i = 90^\circ$ (Lubow et al. 2015). Therefore, a misaligned circumplanetary disc tends to have a larger radius than an aligned disc (see also Miranda & Lai 2015). This may lead to a slight increase in the mass of the circumplanetary disc. We do not expect significant warping to occur in a circumplanetary disc since the sound crossing timescale is much less than the nodal precession timescale (e.g. Larwood et al. 1996; Larwood & Papaloizou 1997; Martin et al. 2014). The tilt of the disc may be higher for lower mass gap-opening planets (Gressel et al. 2013) and their circumplanetary disc may be unstable to tilting as a result of the tidal interaction in the absence of accretion on to the disc (Martin et al. 2020). Since the Galilean satellites are nearly coplanar to Jupiter's orbit around the Sun, it is likely that the circumplanetary disc around Jupiter was close to coplanar.

The mass accretion rate of a circumplanetary disc can be used to predict the radiation flux of a circumplanetary disc. With mock observations, ALMA may detect circumplanetary discs of Jupiter-mass planets at high mass infall rates (Szulágyi et al. 2018; Zhu et al. 2018). The low mass infall rate models in Lubow & Martin (2012) showed that the scale of mass accretion rates are four or five orders of magnitude higher during the outburst phase. However, our models, which include a dead zone and the effect of the tidal torque that drives additional mass transport, show that circumplanetary discs are quite stable and reach a steady state. Thus, if accretion outbursts occur in circumplanetary discs there may be some other mechanism driving them (see Brittain et al. 2020).

6 CONCLUSIONS

We have investigated whether a circumplanetary disc with a dead zone is able to build up sufficient mass for the Galilean satellites to form while remaining sufficiently cool for icy satellites to form. We find that a disc with a dead zone has a higher surface density and similar temperature than a fully MRI turbulent disc. We have modelled the disc evolution and varied parameters including the mass infall rate, the critical surface density required for the dead zone and the viscosity parameter. Material piles up in the dead zone but reaches a steady state that does not undergo accretion outbursts. We find that the tidal torque from the Sun drives an effective viscosity in the dead zone that increases the mass transport rate there. Even with a dead zone, the maximum circumplanetary disc mass reached is around $0.001 M_J$. The disc mass is orders of magnitude smaller than the minimum-mass subnebula model in Mosqueira & Estrada (2003), but consistent with the gas-starved satellite formation model (Canup & Ward 2002; Ward & Canup 2010) and two-dimensional hydrodynamical simulations with radiative cooling in Zhu et al. (2016) that have surface densities in the range of $10 - 1000 \text{ g cm}^{-2}$. Thus the circumjovian disc may not contain sufficient solid material to form the Galilean satellites at any given instant of time. We suggest that solid material must be delivered to the disc rather than in situ

formation of satellitesimals and satellites (e.g. Ronnet et al. 2018).

ACKNOWLEDGEMENTS

The majority of the simulations were run on the Cherry Creek cluster at the UNLV National Supercomputing Institute. This work used the Extreme Science and Engineering Discovery Environment (XSEDE) Stampede2 at the Texas Advanced Computing Center (TACC) through allocation AST130002. CC acknowledges support from a UNLV graduate assistantship. CC thanks Ming-Tai Wu in developing the parallel function on the Cherry Creek cluster and is grateful to Pin-Gao Gu and Min-Kai Lin for helpful comments and inspiring conversations. CCY is grateful for the support from NASA via the Emerging Worlds program (Grant #80NSSC20K0347). We acknowledge support from NASA TCAN award 80NSSC19K0639.

DATA AVAILABILITY

The data underlying this article will be shared on reasonable request to the corresponding author.

REFERENCES

- Adachi I., Hayashi C., Nakazawa K., 1976, *Progress of Theoretical Physics*, 56, 1756
- Armitage P. J., Livio M., Pringle J. E., 2001, *MNRAS*, 324, 705
- Artymowicz P., Lubow S. H., 1996, *ApJ*, 467, L77
- Ayliffe B. A., Bate M. R., 2009, *MNRAS*, 393, 49
- Bai X.-N., Goodman J., 2009, *ApJ*, 701, 737
- Bai X.-N., Stone J. M., 2010, *ApJ*, 722, 1437
- Bai X.-N., Stone J. M., 2013, *ApJ*, 769, 76
- Balbus S. A., Hawley J. F., 1991, *ApJ*, 376, 214
- Baruteau C., et al., 2014, in Beuther H., Klessen R. S., Dullemond C. P., Henning T., eds, *Protostars and Planets VI*. p. 667 ([arXiv:1312.4293](https://arxiv.org/abs/1312.4293)), doi:10.2458/azu_uapress_9780816531240-ch029
- Bate M. R., Lubow S. H., Ogilvie G. I., Miller K. A., 2003, *MNRAS*, 341, 213
- Bell K. R., Lin D. N. C., 1994, *ApJ*, 427, 987
- Benítez-Llambay P., Masset F. S., 2016, *ApJS*, 223
- Birnstiel T., Ormel C. W., Dullemond C. P., 2011, *A&A*, 525, A11
- Bodo G., Cattaneo F., Mignone A., Rossi P., 2014, *ApJ*, 787, L13
- Brittain S. D., Najita J. R., Dong R., Zhu Z., 2020, *arXiv e-prints*, p. [arXiv:2003.11980](https://arxiv.org/abs/2003.11980)
- Canup R. M., Ward W. R., 2002, *AJ*, 124, 3404
- Canup R. M., Ward W. R., 2006, *Nature*, 441, 834
- Collins T. J. B., Helfer H. L., Van Horn H. M., 1998, *ApJ*, 502, 730
- D'Angelo G., Henning T., Kley W., 2002, *A&A*, 385, 647
- D'Angelo G., Henning T., Kley W., 2003, *ApJ*, 599, 548
- Davies R. I., et al., 2010, in Peterson B. M., Somerville R. S., Storch-Bergmann T., eds, *IAU Symposium Vol. 267*, IAU Symposium. pp 283–289 ([arXiv:0911.4355](https://arxiv.org/abs/0911.4355)), doi:10.1017/S1743921310006496
- Dutrey A., et al., 2014, in Beuther H., Klessen R. S., Dullemond C. P., Henning T., eds, *Protostars and Planets VI*. p. 317 ([arXiv:1402.3503](https://arxiv.org/abs/1402.3503)), doi:10.2458/azu_uapress_9780816531240-ch014

- Estrada P. R., Mosqueira I., Lissauer J. J., D'Angelo G., Cruikshank D. P., 2009, in Pappalardo R. T., McKinnon W. B., Khurana K. K., eds, Europa. Univ. Arizona Press, Tucson, AZ, p 27
- Fleming T., Stone J. M., 2003, *ApJ*, 585, 908
- Fromang S., Papaloizou J., Lesur G., Heinemann T., 2007, *A&A*, 476, 1123
- Fujii Y. I., Okuzumi S., Tanigawa T., Inutsuka S.-i., 2014, *ApJ*, 785, 101
- Fujii Y. I., Kobayashi H., Takahashi S. Z., Gressel O., 2017, *AJ*, 153, 194
- Gammie C. F., 1996, *ApJ*, 457, 355
- Gammie C. F., Menou K., 1998, *ApJ*, 492, L75
- Goldreich P., Sari R., 2003, *ApJ*, 585, 1024
- Goldreich P., Tremaine S., 1979, *ApJ*, 233, 857
- Goldreich P., Tremaine S., 1980, *ApJ*, 241, 425
- Gressel O., Nelson R. P., Turner N. J., 2011, *MNRAS*, 415, 3291
- Gressel O., Nelson R. P., Turner N. J., Ziegler U., 2013, *ApJ*, 779, 59
- Hawley J. F., Gammie C. F., Balbus S. A., 1995, *ApJ*, 440, 742
- Hayashi C., 1981, *Progress of Theoretical Physics Supplement*, 70, 35
- Johansen A., Klahr H., Mee A. J., 2006, *MNRAS*, 370, L71
- King A. R., Pringle J. E., Livio M., 2007, *MNRAS*, 376, 1740
- Klahr H. H., Bodenheimer P., 2003, *ApJ*, 582, 869
- Kley W., 1999, *MNRAS*, 303, 696
- Kuskov O. L., Kronrod V. A., 2005, *Icarus*, 177, 550
- Lambrechts M., Johansen A., 2012, *A&A*, 544, A32
- Larwood J. D., Papaloizou J. C. B., 1997, *MNRAS*, 285, 288
- Larwood J. D., Nelson R. P., Papaloizou J. C. B., Terquem C., 1996, *MNRAS*, 282, 597
- Lecar M., Podolak M., Sasselov D., Chiang E., 2006, *ApJ*, 640, 1115
- Lesur G., Ogilvie G. I., 2010, *MNRAS*, 404, L64
- Lin D. N. C., Pringle J. E., 1987, *MNRAS*, 225, 607
- Lubow S. H., D'Angelo G., 2006, *ApJL*, 641, 526
- Lubow S. H., Ida S., 2010, in Seager S., ed., *Exoplanets*. Univ. Arizona Press, Tucson, AZ, p 347-371.
- Lubow S. H., Martin R. G., 2012, *ApJL*, 749, L37
- Lubow S. H., Martin R. G., 2013, *MNRAS*, 428, 2668
- Lubow S. H., Seibert M., Artymowicz P., 1999, *ApJ*, 526, 1001
- Lubow S. H., Martin R. G., Nixon C., 2015, *ApJ*, 800, 96
- Lunine J. I., Stevenson D. J., 1982, *Icarus*, 52, 14
- Lyra W., Klahr H., 2011, *A&A*, 527, A138
- Machida M. N., Kokubo E., Inutsuka S.-i., Matsumoto T., 2008, *ApJ*, 685, 1220
- Martin R. G., Livio M., 2012, *MNRAS*, 425, L6
- Martin R. G., Lubow S. H., 2011, *ApJ*, 740, L6
- Martin R. G., Lubow S. H., 2014, *MNRAS*, 437, 682
- Martin R. G., Lubow S. H., Livio M., Pringle J. E., 2012a, *MNRAS*, 420, 3139
- Martin R. G., Lubow S. H., Livio M., Pringle J. E., 2012b, *MNRAS*, 423, 2718
- Martin R. G., Nixon C., Lubow S. H., Armitage P. J., Price D. J., Doğan S., King A., 2014, *ApJL*, 792, L33
- Martin R. G., Nixon C. J., Pringle J. E., Livio M., 2019, *New Astron.*, 70, 7
- Martin R. G., Zhu Z., Armitage P. J., 2020, *ApJ*, 898, L26
- Meheut H., Fromang S., Lesur G., Joos M., Longaretti P.-Y., 2015, *A&A*, 579, A117
- Miranda R., Lai D., 2015, *MNRAS*, 452, 2396
- Moraes R. A., Kley W., Vieira Neto E., 2018, *MNRAS*, 475, 1347
- Morbidelli A., Szulágyi J., Crida A., Lega E., Bitsch B., Tanigawa T., Kanagawa K., 2014, *Icarus*, 232, 266
- Mosqueira I., Estrada P. R., 2003, *Icarus*, 163, 198
- Ochi Y., Sugimoto K., Hanawa T., 2005, *ApJ*, 623, 922
- Ogilvie G. I., Lubow S. H., 2003, *ApJ*, 587, 398
- Oishi J. S., Mac Low M.-M., 2009, *ApJ*, 704, 1239
- Oishi J. S., Mac Low M.-M., 2011, *ApJ*, 740, 18
- Oishi J. S., Mac Low M.-M., Menou K., 2007, *ApJ*, 670, 805
- Okuzumi S., Hirose S., 2011, *ApJ*, 742, 65
- Okuzumi S., Tanaka H., Kobayashi H., Wada K., 2012, *ApJ*, 752, 106
- Paardekooper S. J., 2007, *A&A*, 462, 355
- Paardekooper S. J., Mellema G., 2006, *A&A*, 453, 1129
- Petersen M. R., Julien K., Stewart G. R., 2007, *ApJ*, 658, 1236
- Pierens A., Nelson R. P., 2010, *A&A*, 520, A14
- Pollack J. B., Lunine J. I., Tittmore W. C., 1991, in Bergstrahl J. T., Miner E. D., Matthews M. S., eds, *Uranus*. Univ. Arizona Press, Tucson, AZ, p. 469
- Quillen A. C., Trilling D. E., 1998, *ApJ*, 508, 707
- Ronnet T., Mousis O., Vernazza P., Lunine J. I., Crida A., 2018, *AJ*, 155, 224
- Ryan B. R., Gammie C. F., Fromang S., Kestener P., 2017, *ApJ*, 840, 6
- Sano T., Miyama S. M., Umebayashi T., Nakano T., 2000, *ApJ*, 543, 486
- Sato T., Okuzumi S., Ida S., 2016, *A&A*, 589, A15
- Schubert G., Anderson J. D., Spohn T., McKinnon W. B., 2004, in Bagenal F., Dowling T. E., McKinnon W. B., eds, *Jupiter. The Planet, Satellites and Magnetosphere*, Vol. 1. Cambridge Univ. Press, Cambridge, p. 281
- Shakura N. I., Sunyaev R. A., 1973, *A&A*, 24, 337
- Shi J.-M., Chiang E., 2014, *The Astrophysical Journal*, 789, 34
- Shibaike Y., Ormel C. W., Ida S., Okuzumi S., Sasaki T., 2019, *arXiv e-prints*, p. arXiv:1909.00285
- Soon K.-L., et al., 2019, *PASJ*, 71, 124
- Suzuki T. K., Muto T., Inutsuka S.-i., 2010, *ApJ*, 718, 1289
- Suzuki T. K., Ogihara M., Morbidelli A. r., Crida A., Guillot T., 2016, *A&A*, 596, A74
- Szulágyi J., Morbidelli A., Crida A., Masset F., 2014, *ApJ*, 782, 65
- Szulágyi J., Plas G. v. d., Meyer M. R., Pohl A., Quanz S. P., Mayer L., Daemgen S., Tamburello V., 2018, *MNRAS*, 473, 3573
- Tanigawa T., Ohtsuki K., Machida M. N., 2012, *ApJ*, 747, 47
- Turner N. J., Sano T., 2008, *ApJ*, 679, L131
- Turner N. J., Sano T., Dziourkevitch N., 2007, *ApJ*, 659, 729
- Umebayashi 1983, *Progress of Theoretical Physics*, 69, 480
- Umebayashi T., Nakano T., 1981, *PASJ*, 33, 617
- Uribe A. L., Klahr H., Flock M., Henning T., 2011, *ApJ*, 736, 85
- Uribe A. L., Klahr H., Henning T., 2013, *ApJ*, 769, 97
- Walker J., Lesur G., Boldyrev S., 2016, *MNRAS*, 457, L39
- Ward W. R., 1997, *Icarus*, 126, 261
- Ward W. R., Canup R. M., 2010, *AJ*, 140, 1168
- Yang C.-C., Mac Low M.-M., Menou K., 2009, *ApJ*, 707, 1233
- Yang C.-C., Mac Low M.-M., Johansen A., 2018, *ApJ*, 868, 27
- Youdin A. N., Lithwick Y., 2007, *Icarus*, 192, 588
- Youdin A. N., Shu F. H., 2002, *ApJ*, 580, 494
- Zhu Z., Hartmann L., Calvet N., Hernandez J., Muzerolle J., Tannirkulam A.-K., 2007, *ApJ*, 669, 483
- Zhu Z., Hartmann L., Gammie C., 2009, *ApJ*, 694, 1045
- Zhu Z., Nelson R. P., Dong R., Espaillat C., Hartmann L., 2012, *ApJ*, 755, 6
- Zhu Z., Ju W., Stone J. M., 2016, *ApJ*, 832, 193
- Zhu Z., Andrews S. M., Isella A., 2018, *MNRAS*, 479, 1850
- Zsom A., Ormel C. W., Dullemond C. P., Henning T., 2011, *A&A*, 534, A73

This paper has been typeset from a \LaTeX file prepared by the author.